

POLITECNICO
MILANO 1863

RE.PUBLIC@POLIMI
Research Publications at Politecnico di Milano

Post-Print

This is the accepted version of:

S. Ghiasvand, A. Airoldi, P. Bettini, C. Mirani
Analysis of Residual Stresses and Interface Damage Propagation in Hybrid Composite/metallic Elements Monitored Through Optical Fiber Sensors
Aerospace Science and Technology, Vol. 129, 2022, 107373 (15 pages)
doi:10.1016/j.ast.2022.107373

The final publication is available at https://doi.org/10.1016/j.ast.2022.107373

Access to the published version may require subscription.

When citing this work, cite the original published paper.

© 2022. This manuscript version is made available under the CC-BY-NC-ND 4.0 license
http://creativecommons.org/licenses/by-nc-nd/4.0/

Permanent link to this version
http://hdl.handle.net/11311/1201465

Analysis of residual stresses and interface damage propagation in hybrid composite/metallic elements monitored through optical fiber sensors

S. Ghiasvand [a,b,*], A. Airoldi [a], P. Bettini [a], C. Mirani [a]

[a] Department of Aerospace Science and Technology, Politecnico di Milano - Via La Masa 34, Milano 20156, Italy
[b] Department of Engineering, University of Liverpool, Liverpool, L69 3GH, United Kingdom

A B S T R A C T

The presence of residual stresses due to the manufacturing process may influence the development of damage in the interfaces of hybrid composite/metallic elements, thus complicating the structural integrity analysis. The paper presents an integrated experimental and numerical approach to develop sufficiently accurate models for the residual stress build-up and the interface damage propagation in hybrid structures. The experimental part focuses on the effect of residual thermal stress on mode I fracture behavior in three different interfaces of co-bonded composite/metallic hybrid specimens under the DCB test. The strain evolution is monitored by FBG sensors carried by optical fibers embedded in the specimens during the manufacturing and DCB test. Strain evolution during the curing cycle is used to calibrate a cooling simulation, followed by the simulation of the mechanical tests. The resulting multistep numerical approach obtains an appreciable correlation with experimental forces, strain evolution, and final residual strain in the DCB tests. Experimental and numerical analyses indicate that residual thermal stress can affect the evolution of strains during crack propagation, the development of permanent displacements, and the forces required to propagate the cracks.

1. Introduction

Although composite materials have become a preferred solution for highly efficient lightweight structures, elements based on the combination of metallic and composite parts are often used to overcome typical limitations of composites, such as poor properties in three-dimensional stress states and low working temperature, as well as to mitigate the effects of damage development in composite plies. Nowadays, hybrid metallic/composite components play essential roles in many high-performance structural applications in several industrial fields (e.g., aerospace, automotive, wind energy, etc.), and the diffusion of additive manufacturing techniques for the production of metallic parts with complex geometries suggests the possibility of more future applications. Currently, a significant example is represented by Fiber Metal Laminates (FML), which have superior fatigue and damage tolerance performances with respect to metal sheets or composite laminates, if considered separately [1]. Furthermore, metal inserts may also be used in composites at the locations of load introduction, like in [2], to improve the structural efficiency in composite joints, as studied in [3,4], or to develop highly efficient solutions for parts that are traditionally made of metallic materials, such as torque shafts [5,6]. In these engineering applications, the joining between metallic elements and composite plies can be obtained through different techniques, such as the secondary bonding between a cured composite part and a metallic part or the co-curing of the composite plies to the metallic element, with or without the use of an adhesive interface. A description of possible alternatives to joining composite and metallic parts is presented in [7]. In all the cases, due to the significantly different Coefficient of Thermal Expansions (CTE's) between metal and composite plies, residual thermal stresses arise and may have detrimental effects on the mechanical performance of the hybrid element. This also motivated the development of special curing cycles to reduce the residual stress levels in hybrid elements [8,9].

Since interfaces are a typical weak point of layered structures, an important issue is represented by the effects of residual thermal stresses on the interface fracture toughness of adhesively bonded joints between composite and metallic parts. Currently, only the same adherent materials are considered standard mode I fracture in Double Cantilever Beam (DCB) [10]. However, the fracture

* Corresponding author at: Department of Aerospace Science and Technology, Politecnico di Milano - Via La Masa 34, Milano 20156, Italy.
E-mail address: sara.ghiasvand@polimi.it (S. Ghiasvand).

behavior of the interface could be relevant to both materials of adherents in the hybrid structure which brings the mismatch of CTE and built-in residual thermal stress [11]. The study carried out in [12] indicates that residual stresses may have a considerable influence in determining the Stress Energy Release Rate, SERR, available to open a crack at the bonded interface between dissimilar materials. Analogous results were found in [13], where the effects of residual thermal stresses were evaluated by varying the thickness of adherents in co-cured composite-metallic asymmetric specimens without adhesive. The analytical and numerical studies on bi-material specimens conducted in [14] point out that the strain energy stored in the hybrid structure, related to the residual thermal stress state, leads to the presence of a non-zero energy release rate even when there are no mechanical loads, with effects that depend on both material and specimen geometry. In the metal-composite adhesive joint studied in [15], residual stresses account for almost 30% of the energy release rate in Mode I, considering a DCB test, and even a higher percentage in Mode II tests based on End Notched Flexure (ENF) Specimens.

In general, the consideration of the effects of residual thermal stresses on the interface toughness in hybrid composite/metallic elements has to face several issues, such as the identification of proper experimental methods (i), the development of the analytical or numerical approach to predict the crack propagation under a given load condition (ii), and the evaluation of the reliability in the prediction of the residual stress levels originated in the bonding or co-bonding processes (iii).

Experimental methods represent the first issue since testing of interfaces between dissimilar materials generally requires asymmetric specimens, which complicate the application of data reduction methods to evaluate critical energy release rates and may be characterized by crack openings that develop in mixed modes. The specimen presented in [16] was designed to obtain approximately a pure Mode I characterization since the thicknesses of the arms of a hybrid DCB specimen are chosen considering the bending stiffness of the materials. An approach to consider the mixed-mode crack propagation is also proposed in [15] for asymmetric DCB and ENF specimens. In general, it appears difficult to obtain the desired level of residual stress, control the crack propagation mode of the test, and avoid the onset of inelastic phenomena, such as yielding or damage development in the metallic and composite layers during the test.

Considering the second of the issues mentioned above, the assessment of residual thermal stresses and the analysis of crack propagation in the presence of residual stress, various analytical approaches have developed. In the last decade, the theory of inverse methods such as the stress function [17–19] and smoothed inverse eigenstrain [20,21] have been established to evaluate residual thermal stress based on limited experimental measurements. These methods propose a technique for reconstructing the residual stress and eigenstrain fields. Furthermore, the impact of the residual stress field on crack propagation for generic layered plates, including interfaces in composite orthotropic laminates with non-homogeneous lay-ups, is studied by several authors [22–25]. However, the assessment of general and practical numerical methods for thermal stress build-up and damage propagation analyses is of fundamental importance for application to real-world cases, with complex geometry, lay-up, load conditions, and damage scenarios.

Both analytical and numerical approaches require a reliable evaluation of residual stress levels, representing a third fundamental issue in consideration of residual stress effects. Such a task is typically performed by assuming constant CTE's to calculate the thermal stress build-up in the cooling phase of the process through a linear thermo-elastic analysis. Moreover, the analysis of the cooling phase requires the choice of an initial stress-free temperature, which is often approximated by using the glass transition temperature or the curing temperature of the material [5,6,12,14,23–25]. Although such assumptions may lead to acceptable results, this kind of approach should be validated through specific tests [26]. Since a reliable evaluation of residual thermal stress in composite structures could require more complex numerical analyses, considering the effects of geometry, tool friction, chemical shrinkage of the resin, CTE's variability, general viscoelastic effects in the resin [27–29], and vibration in resin solidification [30–32]. These uncertainties in evaluating residual stress levels could be reduced by monitoring the curing process using an advanced diagnostic technique.

All the aforementioned considerations suggest that the characterization and the modeling of the effects of residual thermal stresses on the response of hybrid composite-metallic structural elements involve multi-disciplinary aspects related to engineering considerations, experimental methods, analytical and numerical approaches. It is also apparent that the possibility to monitor the stress-strain development during the curing process and the propagation of a crack would provide substantial aid in the calibration and validation of the numerical methods. This paper is aimed to investigate the role of residual thermal stress in the interfaces and the interlaminar layers of composite/metallic specimens and to present experimental and numerical procedures, including strain monitoring, to develop reliable models for the prediction of crack propagation. Overall, such a goal was accomplished by using pre-cracked layered hybrid specimens, which were first used to characterize the propagation of a crack propagating in Mode I at an interface without any effect of residual thermal stress. Then, specimens with the same lay-up but with pre-cracks introduced at different interfaces/interlaminar layers were used to perform tests in the presence of residual thermal stress effects on the energy release rate.

A diagnostic technique based on the embedment of Fiber Bragg Grating (FBG) sensors carried by optical fibers was applied to monitor the curing process. Such a technique, which makes possible the development of a lightweight and efficient strain sensing network [33,34], has already been applied to follow the development of the strains during the curing of composites and FML's by several authors [35–43]. In this work, the same sensors were used to monitor the curing cycle and then fracture mechanic tests in DCB configuration, investigating the strain evolution during the crack propagation.

The tests and the data acquired by the strain sensing network made possible the calibration and validation of a numerical procedure, based on a thermal analysis followed by the simulation of crack propagation performed by applying a Cohesive Zone Model (CZM) following the technique presented in [44–46]. Numerical analyses were conducted with and without considering the thermal stress induced by the curing process. Results were correlated with force vs. displacement response and the internal strains acquired by FBG sensors embedded in the composite layers.

The paper is organized into five sections, including this introduction. In the next section, the technological and experimental activities are presented. In the third section, the CZM and the overall numerical approach are illustrated. In the subsequent fourth section, the thermal analyses are calibrated through the correlation with FBG's data; then, the models are applied to the analysis of the fracture tests, presenting the correlations with force vs. displacement curves and with the internal strains acquired by the FBG's. Finally, the main findings of the activity are summarized in a final concluding fifth section.

Table 1
Mechanical properties of materials.

		AS4/8552[1] [48]	Titanium Ti-6AL-4V [49]	3MTM Scotch-AFK-163-2K [50]
Young Moduli (MPa)	E	$E_{11} = 127277$ $E_{22} = E_{33} = 9239$	114000	1110
Poisson's ratios	v	$v_{12} = v_{13} = 0.302$ $v_{23} = 0.3$	0.34	0.34
Shear Moduli (MPa)	G	$G_{12} = G_{13} = 4826$ $G_{23} = 3553$	42537	414.17
Cured Thickness (mm)	t	0.13 (per ply)	$thin = 1.27$ mm $thick = 2.54$ mm	$t_a = 0.1$ (film)

[1] Both the Federal Aviation Administration (FAA) and the European Aviation Safety Agency (EASA) accept composite specification and design values developed using the NCAMP process [47].

2. Experiments on hybrid specimens with embedded optical fibers

2.1. Design of hybrid specimens to control residual stress effects

In this work, co-bonded interfaces between layers of Ti-6AL-4V titanium alloy and sub-laminates made of AS4/8552 carbon-epoxy composite unidirectional prepregs were considered and tested by using Double Cantilever Beam (DCB) specimens, designed following the ASTM D5528 standard as a guideline [10]. Bonding at all the hybrid composite/metallic interfaces was obtained by co-curing a film of 3MTM Scotch-Weld AFK-163-2K supported adhesive. To increase the adhesion between the adhesive layer and the metal sheet, titanium surfaces were anodized. A list of the most relevant properties and the related references for the materials adopted in the experiments presented in this paper are given in Table 1.

The layered specimens adopted in this work were designed to control the effects of residual thermal stress in manufacturing and crack propagation. The first objective was to characterize the adhesive interface between the metallic layers and the composite sub-laminates without introducing geometrical distortions and effects on the energy release rate due to the build-up of residual thermal stress. To accomplish such an objective, the specimen was designed by considering the following requirements:

a) Both arms of the DCB hybrid specimen were based on symmetric lay-ups to avoid bending-extension coupling in each arm separated by the central interface layer;
b) Equalization of overall CTE by using the same volumetric fraction of composite and titanium alloy in both arms to prevent the distortion of the whole specimen in the curing process;
c) Limitation of the differences between the bending moduli of the arms to obtain an almost symmetric bending in each arm and minimize the influence of Mode II propagation in the DCB tests.

The fulfillment of such requirements led to the specimen shown in Fig. 1-A, which will be defined as a Symmetrically Cracked (SC) specimen. In this specimen, composite sub-laminates had a thickness $t_c = 7 \times 0.13 = 0.91$ mm, obtained with a $[0]_7$ lay-up. Two types of titanium alloy sheets were used: a thin one, with a thickness $t_{ti} = 1.27$ mm, and a thick one, with a thickness $2t_{ti} = 2.54$ mm. As shown in Fig. 1-A, the upper arms consist of two CFRP sub-laminates with the thickness of t_c separated by a thick titanium element with a thickness of $2t_{ti}$. The lower arm consists of two thin titanium alloy layers with a thickness of t_{ti}, separated by two composite sub-laminates with a total thickness of $2t_c$.

Both arms of the DCB specimens and the specimen as a whole can be considered orthotropic laminates with a response that can be analyzed by applying the Classical Lamination Theory (CLT), including the thermal stress developed in the cooling process. This leads to the constitutive equation reported in Eq. (1), which is characterized by the classical ABD matrix [51].

$$\begin{Bmatrix} \{N\} \\ \{M\} \end{Bmatrix} = \begin{bmatrix} [A] & [B] \\ [B] & [D] \end{bmatrix} \begin{Bmatrix} \{\varepsilon_0\} \\ \{\kappa\} \end{Bmatrix} + \begin{Bmatrix} \{N\}^{thermal} \\ \{M\}^{thermal} \end{Bmatrix} \tag{1}$$

Vectors $\{N\}$ and $\{M\}$ in Eq. (1) are the force and moment per unit width acting on the laminate, whereas $\{\varepsilon_0\}$ and $\{\kappa\}$ are the in-plane strains at the mid-plane of the laminate and the curvatures. The thermal forces and moment per unit width, $\{N\}^{thermal}$ and $\{M\}^{thermal}$ are evaluated by knowing the CTE's of the layers, following a standard procedure [51].

The CLT approach was used to analyze the response of the Symmetrically Cracked (SC) specimen in Fig. 1-A, by using the mechanical properties in Table 1 and considering the following values for CTE's of composite plies in material axis, α_1 and α_2: $\alpha_1 = 0.13 \cdot 10^{-6}\,°C^{-1}$ and $\alpha_2 = 37.12 \cdot 10^{-6}\,°C^{-1}$ [43]. The CTE of Titanium was set to $9.0 \cdot 10^{-6}\,°C^{-1}$. Results provided a strain $\varepsilon_{0x} = 810.3\mu\varepsilon$ and $\varepsilon_{0y} = 1865.5\mu\varepsilon$ with a $\Delta T = -160\,°C$ for both the upper and lower arms of the specimen, and for the laminate as a whole. In addition, since the arms are individually symmetric, no curvature was obtained for the SC specimen. The term D_{11} in the ABD matrix presented in Eq. (1) was $9.692 \cdot 10^5$ N · mm for the upper arm and $9.946 \cdot 10^5$ N · mm for the lower arm. Such difference in the bending stiffness of the two arms is expected to lead to a relatively small contribution of Mode II opening in the DCB tests.

As confirmed by the CLT model, the SC specimen design aims to eliminate the effects of residual stress on crack propagation. However, the same lay-up, with cracks in different positions, was also used to investigate cases where the residual stress originated in manufacturing and was expected to affect the crack propagation in the interfaces of the layered specimen. In particular, two Asymmetrically Cracked (AC) specimens were produced (Fig. 1-B,C). In the AC#1 specimen, the pre-crack was positioned in an adhesive layer set above the first CFRP sub-laminate from the bottom, thus including one of the thin titanium layers in the upper arm, as shown in Fig. 1-B. In the AC#2 specimen, it was decided to investigate the effects of the residual stress on the crack propagation inside one of the composite sub-laminates. Accordingly, a pre-delamination was introduced in the middle of the first CFRP sub-laminate from the bottom, with a $[0]_{14}$ lay-up. The position of the pre-crack in such specimen is sketched in Fig. 1. According to [52], the distortion induced in a plate by residual thermal stress can be evaluated by Eq. (2).

$$w = -\frac{1}{2}\left(\kappa_x x^2 + \kappa_y y^2 + \kappa_s xy\right) \tag{2}$$

Where κ is the curvature parameter obtained by CLT and x and y are the dimensions of the plate. The expected distortion of each arm separately and as total distortion based on Eq. (2) is presented in Table 2. Moreover, each specimen's in-plane residual thermal

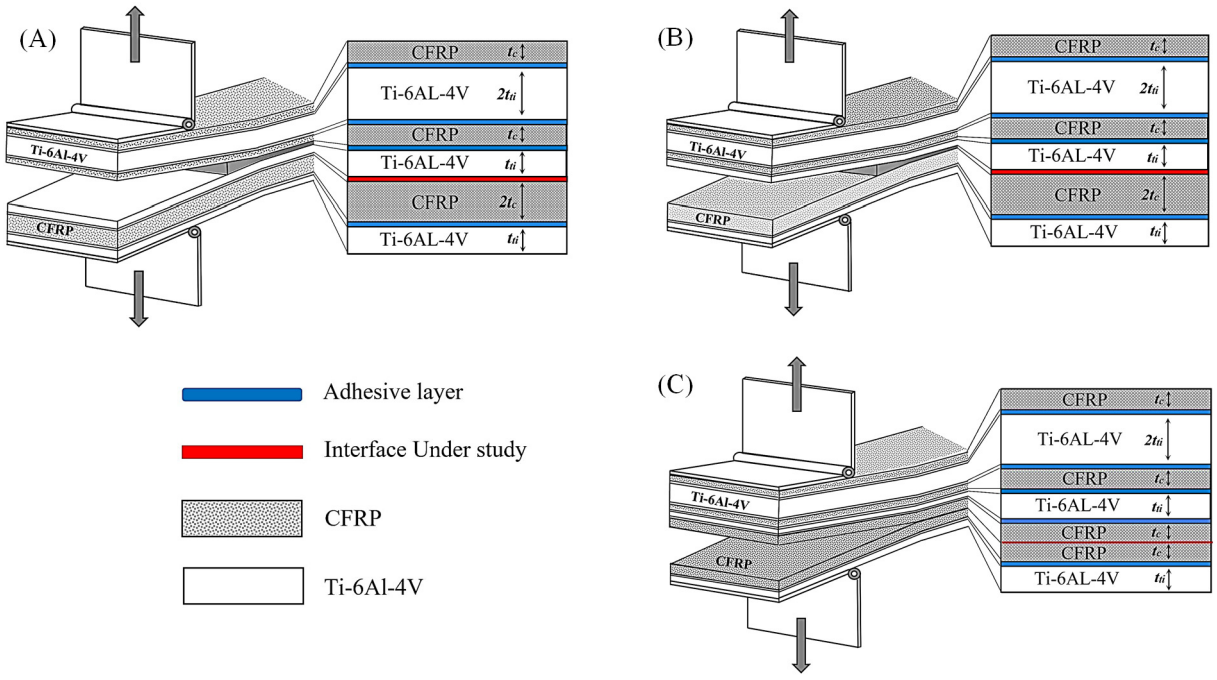

Fig. 1. The lay-up sequences of the hybrid specimens: (A) SC, (B) AC#1, and (C) AC#2 specimens.

Table 2
Distortion and residual stress assessed by CLT of specimens.

Specimen	S_x (MPa)	S_y (MPa)	Distortion down (mm)	Distortion up (mm)	Total distortion down-up (mm)	$\frac{D_{11}^{down}}{D_{11}^{up}}$
SC	27.19	−8.42	0	0	0	≈ 1
AC#1	−37.57	0	1.58	0.27	1.31	0.16
AC#2	−45.98	−23.74	2.06	−0.25	2.31	0.06

stress at the interface layer understudy is also calculated by Eq. (1) and reported in Table 2. It is visible that the residual thermal stress and distortion are rising by increasing the difference between the bending stiffness of arms.

2.2. Lamination of specimens and embedment of optical fibers

Manufacturing of all laminates was carried out by using a hot press plate apparatus, adopting a metallic mold and a countermold. Composite sub-laminates were co-cured to the metallic sheets, and a layer of adhesive was used at each interface between composite and metallic materials. Artificial pre-cracks were introduced by interposing double folded layers of Polytetrafluoroethylene (PTFE) sheets with a thickness of 0.013 mm and a length of 70 mm, in the interfaces selected for SC, AC#1, and AC#2 specimens. It should be observed that even if the 3MTM Scotch-Weld AFK-163-2K adhesive has a curing temperature of about 110 °C [50], it is customarily adopted in the aerospace industry in co-curing processes involving material with different curing temperatures, like the ones adopted in this work. However, the 8552 resin and the adhesive have different glass transition temperatures, and this complicates the definition of a clear zero-stress temperature for the evaluation of residual stress. Such an aspect emphasizes the need for a cure monitoring system embedded in the specimens to calibrate thermal analyses and validate the numerical procedure.

Three specimens were produced for each panel made with the manufacturing process described above. Both panels for the production of SC and AC#1 specimens were equipped with a monitoring system based on Optical Fibers (OF) carrying 3 mm long FBG sensors, which were used to monitor the built-up thermal stress inside the specimens during the manufacturing and its effect on the fracture behavior in the DCB test. FBG sensor is working with the changes in a back-reflected light from Bragg grating [53]. The effective refractive index and periodic spacing on the grating area based on mechanical or thermal follows as Eq. (3).

$$\Delta\lambda_B = \lambda_0\left[\left(\alpha_f + \xi\right)\Delta T + (1 - p_e)\,\Delta\varepsilon\right] = K_T\Delta T + K_\varepsilon\Delta\varepsilon \qquad (3)$$

Where $\Delta\lambda$ and λ_0 are the wavelength shift and Bragg grating's peak reflection wavelength. For the thermal term, α_f, ξ and ΔT are the CTE, Bragg grating's thermo-optical coefficient and temperature change and in mechanical part, p_e is the photoelastic constant of the optical fiber. Which can be considered as the total sensitivity coefficient of K_T and K_ε of the temperature and strain, respectively [53].

The layout of the panel production is shown in Fig. 2-A,B. In this work, a 250 μm diameter OF with a Polyacrylate coating is used. The coating of OF was chemically etched in correspondence of the FBG sensors before the embedment to ensure direct contact between the naked cladding of the OF and the epoxy resin. The optical line denoted as "Sensorized-Naked" in Fig. 2-A,B, was placed in the composite laminate lay-up at a distance of 2 plies from the pre-cracked interface both in SC and AC#1 specimens. The positions of the FBG sensors carried by the fiber in the SC specimen are indicated in Fig. 2-A. In the AC#1 specimen, the fiber was placed in the lower laminate; and the sensors were placed 3 mm closer to the crack tip compare to the SC specimen. The position of the sensors in the AC#1 specimen is shown in Fig. 2-B.

An issue related to monitoring the curing process based on FBG sensors is related to the decoupling of thermal and mechanical measurements (Eq. (3)). Indeed, the sensor measurement is based

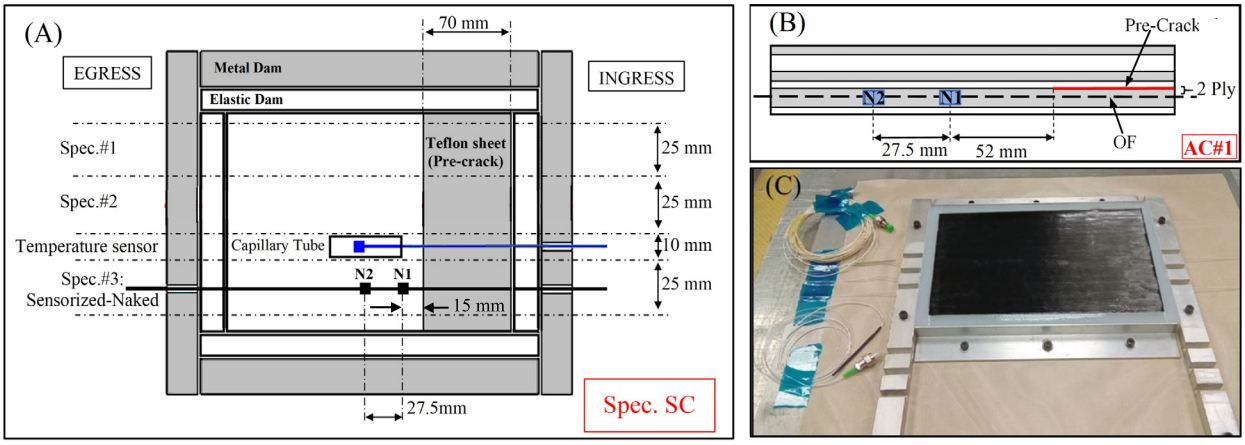

Fig. 2. Sensing network and position of FBGs in SC panel (A), the position of FBG sensors in AC#1 laminate (B), and (C) lamination and embedment of fibers before curing.

on the wavelength shift of the light reflected by the grid of FBG, which is sensitive to both temperature and strain. Following the work presented in [33,40], the method adopted to decouple the strain and temperature signals in this work was based on the embedment of a small capillary tube in the composite, which hosts an FBG sensor measures only the temperature. Accordingly, a third OF was embedded in both panels laminated for SC and AC#1 specimen production, as exemplified in Fig. 2-A. Such optical line was endowed with a sensor that was loosely implanted inside a steel capillary tube. The OF and the tube were embedded in the sub-laminates in the same interface hosting the other FBG sensors in a region that was subsequently removed in the cutting of the DCB specimens. Assuming a uniform temperature in the plane of the interface that hosts all the sensors, the temperature signal obtained by FBG sensors inside the capillary tube can be subtracted by the signals acquired by the other sensors, so to decouple the measure of strain from the temperature.

In the technological process, the resin loss from the edges was controlled by using a frame of silicon rubber, which was featured with passages for optical fibers. Such frame was inserted in a secondary frame made of metallic dams. The mold assembly is shown in Fig. 2-C. The ingress and egress of fibers from the panels were protected by PTFE tubes, which were partially embedded at the laminate border and passed through the silicon frame. The laminate for the production of the SC and AC#1 specimens had a width of 125 mm and a length of 200 mm. A smaller laminate, without the embedment of the OF-based sensing network, was prepared for the AC#2 specimens, with a width of 65 mm and a length of 200 mm.

2.3. Manufacturing and monitoring of curing cycle

The curing cycle follows the Manufacturer's Recommended Cure Cycle (MRCC) [48]. It involved initial heating until 100 °C, a permanence at such temperature for 1 hour, followed by a second heating phase at the temperature of 180 °C, which was maintained for 2 hours. A final cooling phase until the ambient temperature concluded the cycle. The evolution of temperature and strains inside the SC and AC#1 specimens are shown in Fig. 3, as measured by the FBG sensors in the three optical lines embedded in each panel. The temperature was directly measured by the FBG's positioned in the capillary tube, and it followed quite accurately the evolution imposed to accomplish the cycles. The wavelength shifts of the FBG's in the capillary tube were subtracted from the ones of other sensors so to provide a strain measure.

In the results reported in Fig. 3-A, referred to the SC specimen, the sensors in the optical line experienced a negative strain shift during the initial phase of the heating step caused by pressure. Then, the strains remained stable during the first temperature plateau and exhibited a slightly irregular trend as the temperature was raised until 180 °C. During the second plateau, at 180 °C, negative strains were accumulated. This trend refers to chemical cure shrinkage, which can be observed as a consequence of curing reactions [43,54–56]. Cure shrinkage is referred to polymerization of thermoset resin by significant increase in density and reduction of volume [57]. Finally, in the cooling phase, the behavior was characterized by the development of significant negative strains.

In the manufacturing of the panels for the AC#1 specimens, an attempt was performed to remove possible tensions in the optical fiber, which could have originated during the closure of the mold. The heating step was arrested at about 55 °C, and the mold was open and then re-closed (this period is shown as "No Pressure" in Fig. 3-B). This actually produced significant initial oscillations of the strain signals. Still, despite such an irregular start, the response during the second plateau and the cooling phase was very similar to that of the SC specimen.

After manufacturing, specimens with a width of 25 mm and a length of 200 mm were cut from the panels and prepared for DCB tests. All the cuts were carried out using a water jet cutter and involved removing the stripes that contained the capillary tubes. Three specimens were cut from the SC and the AC#1 panel, following the scheme presented in Fig. 2-A. Two of these specimens remained equipped with naked sensors (Spec.#3-SC and Spec.#2-AC#1). Two specimens without sensors were cut from the smaller panels for the production of AC#2 specimens. As expected from the design phase, after the cutting operations, the SC specimens did not exhibit any curvature and distortion (Fig. 4-A), thus confirming analytical predictions. On the contrary, curvatures were obtained in the pre-cracked region both for AC#1 and AC#2 specimens, as shown in Fig. 4-B,C. Indeed, the contraction of the titanium sheet on the lower arms induced a curvature that opened the pre-crack in both laminates, as is particularly evident in AC#2 specimens (Fig. 4-C).

2.4. DCB experimental tests

The pictures reported in Fig. 5 are related to the DCB tests performed on the three types of specimens manufactured as described in the previous sections. An MTS 858 hydraulic test system was used for all the experiments at room temperature conditions. According to ASTM D 5528-13 [10] procedure, specimens were subjected to a pre-opening procedure to obtain a crack tip representative of a fracture process evolving in real operational conditions. In the pre-opening phase, the specimens were loaded until a

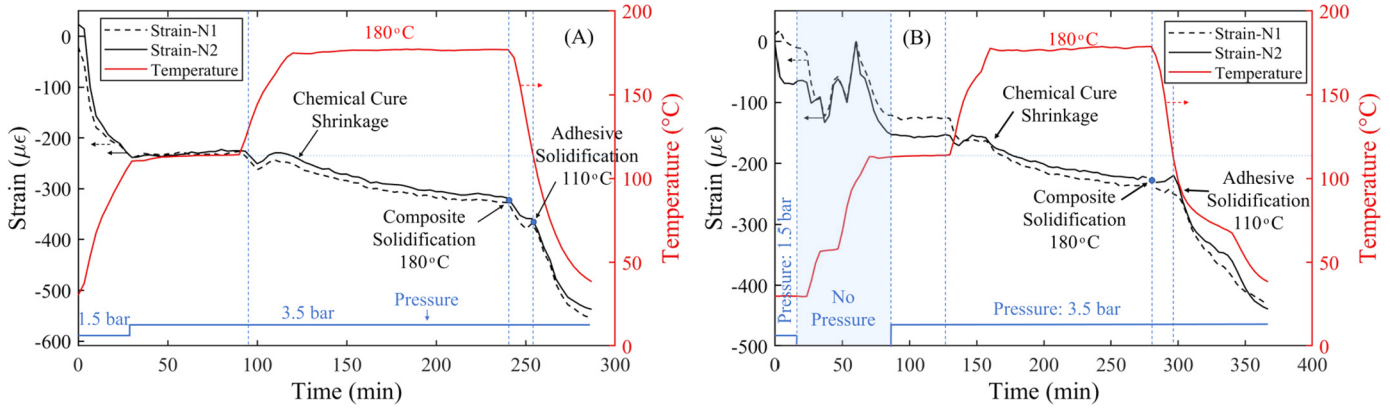

Fig. 3. Temperature and strain evolution during the curing phases in SC (A) and AC#1 (B) specimens measured by FBG sensors.

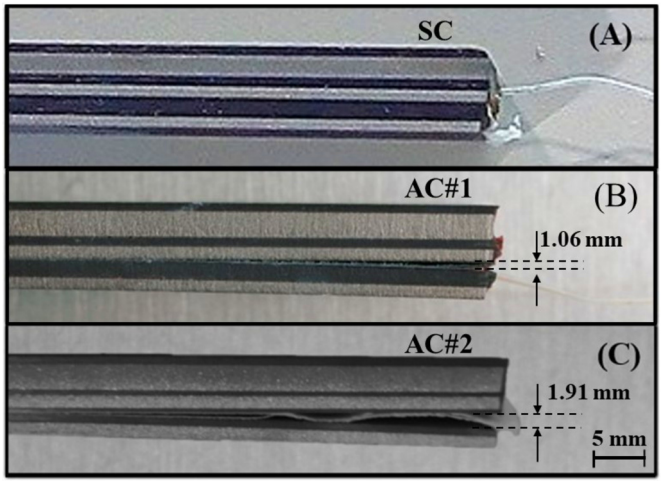

Fig. 4. Comparison of A) SC, B) AC#1, and C) AC#2 specimen after manufacturing and waterjet cut.

crack propagation of about 5 mm. After unloading, the main loading phase followed. The edges of all the specimens were painted with a white coating to improve the detectability of the crack tip, and pictures were taken at an interval of 10 (sec) during the tests to record the crack advancement.

In the tests performed on SC specimens, The opening mode was apparently in Mode I, as indicated by the horizontal position of the specimen in Fig. 5-A, thanks to the slight differences in the bending stiffness of two arms of the DCB. The response of the three SC specimens is presented in Fig. 6-A. The responses were characterized by appreciable repeatability, and it can be observed that a negligible permanent displacement was obtained at the end of the unloading phase. In the tests performed on the specimens cut from AC#1, the asymmetry of the arms led to incline the laminate during the DCB test, as shown in Fig. 5-B. Two of the tests were subjected to two loading-unloading cycles to check the response of the optical fibers and to investigate the accumulation of residual displacements.

The repeatability was also acceptable in this case, though the specimen with sensors exhibited a smaller force level. A significant residual displacement was obtained at unloading in all the tests, as reported in Fig. 6-B.

The two AC#2 specimens were characterized by the crack development in an interlaminar layer of a composite sub-laminate and by a remarkable asymmetry between the two arms separated by the crack plane. The inclination of the specimens due to such asymmetry is particularly evident in Fig. 5-C. The force levels for the two specimens are reported in Fig. 6-C and are much lower than those obtained for the crack propagation through the adhesive due to the lower interface toughness. In the pre-opening phase, an unstable propagation was observed, and secondary cracks developed in the sub-laminates. However, in the opening phase, the crack propagated only in the pre-damaged interface. It can be observed that the responses of both AC#2 specimens are very similar and characterized by a noticeable, permanent residual displacement at unloading.

During the tests, the internal strains measured by the FBG sensors were acquired in the SC and AC#1 specimens to validate the numerical approach, which will be presented and analyzed in section 5.

For the adhesive interfaces, the absence of distortions and residual displacement confirmed that the residual stress did not influence the response of the SC specimens in the hybrid laminates. Hence, the data reduction methods suggested by the ASTM standard [10] were applied to evaluate a reference value for the Critical Energy Release Rate, G_{Ic}, to be confirmed by numerical analyses. The first one, Modified Beam Theory (MBT), is based on the following formula [10]:

$$G_{Ic} = \frac{3P\delta}{2b\,(a + |\Delta|)} \tag{4}$$

Where P is applied load, δ is the displacement at the load point, b is specimen width, a is the crack length and Δ is a correction parameter for crack tip rotation and deflection and is determined from linear regression analysis of cube root of specimen compliance $C^{1/3}$ versus a. In the case of the Compliance Calibration (CC):

$$G_{Ic} = \frac{nP\delta}{2ab} \tag{5}$$

Here, n is a correction parameter: the slope of $\ln(C)$ versus $\ln(a)$ curve. And finally for the Modified Compliance Calibration (MCC):

$$G_{Ic} = \frac{3P^2C^{2/3}}{2A_1bh} \tag{6}$$

Where A_1 is the slope of squares plot of the delamination length normalized by specimen thickness, a/h, as a function of the cube root of compliance, $C^{1/3}$.

The MBT, CC, and MCC methods were applied to the data reported in Fig. 6-A and the crack evolution evaluated from the pictures taken during the tests. The values of G_{Ic} obtained by the different methods at different crack lengths are reported in Fig. 7-A. Considering the scattering between the methods, an average value of 3.3 kJ/m^2 was chosen to characterize the G_{Ic} value in the numerical procedures.

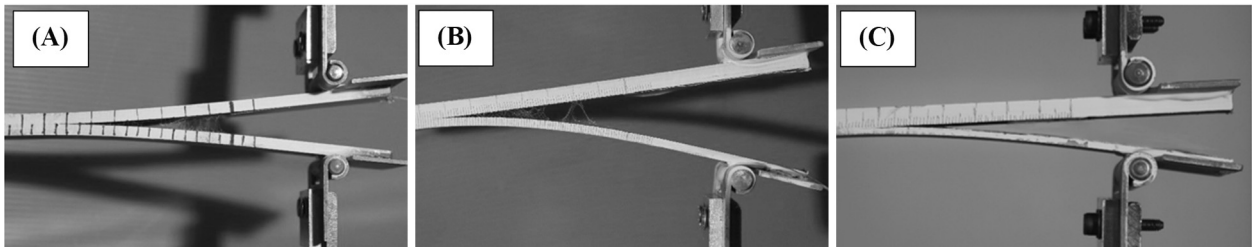

Fig. 5. DCB experiment test of A) SC, B) AC#1, and C) AC#2 specimens.

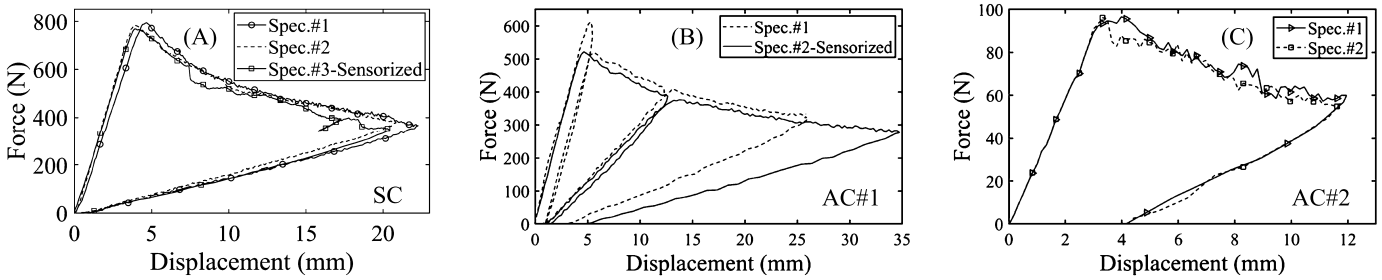

Fig. 6. Force vs. Displacement curves of A) SC, B) AC#1, and C) AC#2 specimens.

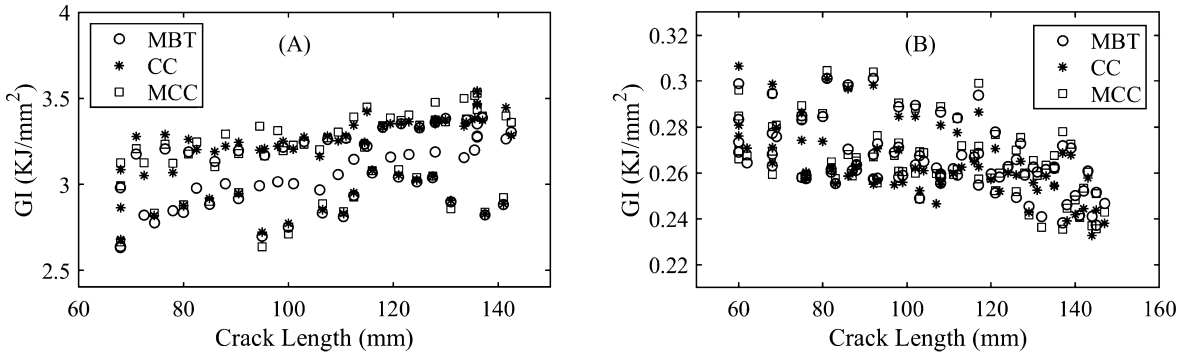

Fig. 7. Experimental R-curves were obtained with three different data reduction methods for (A) SC specimens and (B) unidirectional AS4/8552 interlaminar toughness.

A series of DCB tests were also performed to evaluate the interlaminar toughness in Mode I for the interlaminar layer within the AS4/8552 composite sub-laminates in order to obtain a reference value to be adopted in the analysis of AC#2 specimens. Five specimens were produced with a lay-up sequence of $[0]_{30}$, for a total thickness of about 4 mm, with a width of 25 mm and a length of 250 mm. Experiments were conducted following the ASTM standard [10] and obtained regular and repeatable responses. The values of G_{Ic} obtained by applying the data reduction methods suggested in [10] are reported in Fig. 7-B. The average value of interlaminar toughness for AS4/8552 was found to be 0.26 kJ/mm^2.

3. Numerical models of the hybrid specimens

3.1. Proposed cohesive modeling approach for adhesive layers

The data acquired in the technological and experimental activities were used for the calibration and assessment of a numerical approach capable of reliably predicting the build-up of residual stresses and their global and local effects in the propagation of crack at interfaces in hybrid composite/metallic structures. Modeling of interface damage was based on Cohesive Zone Models (CZM's), which were used to represent the pre-cracked adhesive interfaces in specimens SC and AC#1. In typical implementations, CZM's are defined by non-linear traction-separation laws, which link displacement discontinuities and the out-of-plane stress components transmitted through a zero-thickness idealized interface. However, for the adhesive interfaces, cohesive cracks propagate through a film with a non-infinitesimal thickness [58]. Moreover, the adhesive material can transmit in-plane stress components and has a thermo-mechanical response, which is characterized by specific CTE values. Thus, in-plane stress components and thermal behavior may influence the state of stress in the adhesive in hybrid laminates. For such a reason, a CZM was included infinite thickness solid elements, with a complete three-dimensional stress-strain response in the elastic range and the possibility to represent thermal strains.

This approach is already presented in previous papers of the author [44–46,59] and will be briefly discussed in this section. A fundamental aspect of the approach followed for the adhesive is the possibility to describe the fracture processes in Mode I, II, and III by using the components of a vector of relative displacements, Δ, between the faces of two adherends, connected by an adhesive layer of finite thickness t_a. A sketch of a DCB specimen is shown in Fig. 8-A. If the adhesive is represented by using a single layer of hexahedral elements with a reduced integration scheme, the difference Δ, between the displacement $\boldsymbol{U}^+$ and $\boldsymbol{U}^-$ of the adherend faces, is related to the out-of-plane strain state in the integration point of the elements (Fig. 8-A). This leads to Eq. (7), which is valid under a small strain assumption.

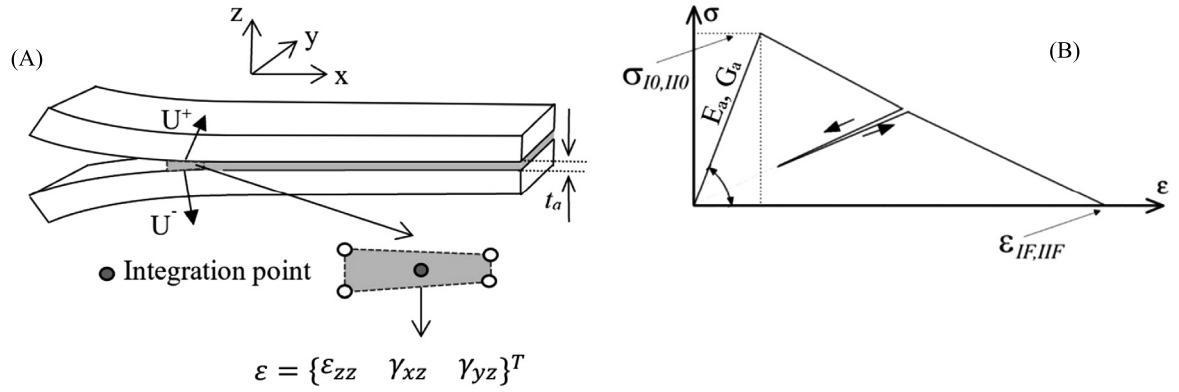

Fig. 8. Embedment of Cohesive Zone Model in a solid layer of adhesive: (A) scheme of a DCB specimen and strain state in an element representing the adhesive, (B) bi-linear constitutive law based on CZM.

$$\Delta = \left\{ \begin{array}{c} \Delta_I \\ \Delta_{II} \\ \Delta_{III} \end{array} \right\} = \left\{ \begin{array}{c} U_z^+ - U_z^- \\ U_x^+ - U_x^- \\ U_y^+ - U_y^- \end{array} \right\} = \left\{ \begin{array}{c} \varepsilon_{zz} \\ \gamma_{xz} \\ \gamma_{yz} \end{array} \right\} t_a \tag{7}$$

In the constitutive law adopted in this paper, the traction-separation law of a CZM was expressed in terms of the Δ components, exploiting Eq. (7). This made possible a formulation of the model based on the strain components at the integration point of the hexahedral element. Following the model proposed in [4], the assumption of equivalent properties for Mode II and Mode III propagation was introduced. Accordingly, two equivalent strain components were defined to drive the fracture process in the adhesive elements, as in Eq. (8).

$$\varepsilon_I = \left\{ \begin{array}{ll} 0 & \text{if } \varepsilon_{zz} \leq 0 \\ \varepsilon_{zz} & \text{if } \varepsilon_{zz} > 0 \end{array} \right. , \qquad \varepsilon_{II} = \sqrt{\gamma_{xz}^2 + \gamma_{yz}^2} \tag{8}$$

The law was formulated considering two equivalent stress components, σ_I and σ_{II}, and a damage variable, d_a, which was introduced to model the degradation of the stress transmission capability of the adhesive interface in the out-of-plane direction. Hence, the damage is introduced to degrade the stiffness properties, as expressed in Eq. (9):

$$\left\{ \begin{array}{l} E_a' = E_a\,(1 - d_a) \\ G_a' = G_a\,(1 - d_a) \end{array} \right. \tag{9}$$

where E_a' and G_a' are the Young modulus and the shear modulus of the material degraded by the damage variable. Ideally, the damage variable should affect selectively only the out-of-plane stiffness properties, but this would lead to some issues in the presence of large deformations in the adhesive elements. Indeed, large deformations may lead to undesired effects in the complete stress vs. strain response due to the coupling between the out-of-plane stress component σ_{zz} and the in-plane stress components σ_{xx} and σ_{yy}, originated by Poisson's ratio effects (see [44]). However, in the study presented in this work, the capability to model the in-plane stress response of the adhesive material was not considered necessary once the damage developed in the adhesive interface. Accordingly, the isotropic adhesive material is uniformly damaged in all the directions by the damage variable d_a, as formalized in Eq. (9).

Mixed-mode damage propagation in the interface was addressed by introducing proper strength and toughness criteria into the damage evolution algorithm. In particular, following the traction-displacement law presented in [4], which was already adopted in the approaches developed in [44–46,59], a quadratic criterion was used to model the strength in mixed mode crack propagation formulated as in Eq. (10).

$$\left(\frac{\sigma_I}{\sigma_{I0}}\right)^2 + \left(\frac{\sigma_{II}}{\sigma_{II0}}\right)^2 = 1 \tag{10}$$

Where σ_{I0} and σ_{II0} are the strength of the adhesive interface in pure Mode I and Mode II opening, respectively.

A key aspect of CZM's is the capability to model the toughness of the interface by controlling the area under the traction-displacement curve, thus completing the information required to define the bi-linear response shown in Fig. 8-B. Furthermore, in the adaptation of the model into solid elements, a link between the fracture toughness in Mode I and II and the stress vs. strain response of the material model was established considering the relation in Eq. (7) and introducing the thickness of the adhesive layer as a material parameter, thus leading to Eq. (11):

$$\left\{ \begin{array}{l} G_{Ic} = \displaystyle\int_0^{\Delta_{If}} \sigma_I d\Delta_I = t_a \int_0^{\varepsilon_{If}} \sigma_I d\varepsilon_I \\ G_{IIc} = \displaystyle\int_0^{\Delta_{IIf}} \sigma_{II} d\Delta_{II} = t_a \int_0^{\varepsilon_{If}} \sigma_{II} d\varepsilon_{II} \end{array} \right. \tag{11}$$

Where G_{IC} and G_{IIc} are the critical SERR's for pure Mode I and Mode II fracture modes, ε_{If} and ε_{IIf} are the strains at the complete failure of the interface, where $d_a = 1$ (see Fig. 8-B), while Δ_{If} and Δ_{IIf} are the corresponding relative displacements.

For mixed-mode propagation, two toughness criteria were considered. The first is a power-law fracture criterion, which was adopted in the stress vs. strain law presented in [44–46,59] and in the traction-displacement law presented in [4], while the second implements a B-K model [60], which was also introduced in the stress vs. strain law presented in [59]. The power law and the B-K criteria are represented by the expression provided in Eq. (12) and Eq. (13), respectively.

$$\left(\frac{G_I}{G_{Ic}}\right)^{\beta} + \left(\frac{G_{II}}{G_{IIc}}\right)^{\beta} = 1 \tag{12}$$

$$G_I + G_{II} = G_{Ic} + (G_{IIc} - G_{Ic}) \left(\frac{G_{IIc}}{G_{Ic} + G_{IIc}}\right)^{\eta} \tag{13}$$

Where in Eq. (12), for linear energetic criterion, $\beta = 1$ and for quadratic energetic criterion $\beta = 2$, are the most frequently used ones for power law [44], and it is suggested explicitly for adhesive in [61]. In the B-K criterion (Eq. (13)), the curve-fitting parameter η assessed from the MMB test at different mode ratio. Coamanho et al. [62] compared mode-mixity of different types of resins such as tough, brittle, and thermoplastic with both power-law and B-K criteria.

Table 3
Mechanical properties of materials used in Numerical Analysis.

	Tensile strength σ_{I0} (MPa)	Shear strength σ_{II0} (MPa)	Mode I toughness G_{IC} (KN/mm^2)	Mode II toughness G_{IIC} (KN/mm^2)
AS4/8552	18	50	0.26	1.2
3MTM Scotch-AFK-163-2K	50	50	3.3	7.96

The above described CZM was implemented in a constitutive law aimed to represent the complete three-dimensional stress vs. strain response of the adhesive, also in the presence of a cohesive crack propagating in the *x*-*y* plane, as shown in Fig. 8-A. The material model was implemented in a VUMAT subroutine linked to the Simulia/Abaqus Explicit code, including the introduction of the thermal strains due to the CTE of the adhesive, which were subtracted by the total strains before calculating the mechanical response.

3.2. Finite elements models for thermal and mechanical analyses

The models of the three-layered specimens presented in section 3 were developed to be analyzed with Simulia/Abaqus Explicit solver. Hexahedral solid elements with a reduced integration scheme (Type *C3D8R* [63]) were used for the composite sub-laminates and the Titanium layers, with a typical size of $0.5 \times 0.5 \times 0.75$ mm^3. They were characterized by using linear elastic material models, with the stiffness properties reported in Table 1. The thermo-mechanical response was modeled by using constant CTE, which was calibrated and assessed considering the results of curing cycle monitoring. The same type of elements and material models were used to represent the 0.1 mm thick layers of adhesive without pre-cracks, which were introduced at any interface between metallic sheets and composite sub-laminates, as in the physical laminates. The elastic linear model of the adhesive was calibrated according to the properties presented in Table 1, as well.

In the models of SC and AC#1 specimens, hexahedral elements with a reduced integration scheme (C3D8R [63]) and the thickness of 0.1 mm were used for the pre-cracked adhesive layers, introducing the material law based on the CZM presented in the previous sub-section 4.1. In the model representing the AC#2 specimens, conventional cohesive elements (Type *COH3D8* [63]) represent the delamination within the composite sub-laminate by selecting the same type of strength and toughness criteria used for the adhesive layers, though calibrated with different values. Indeed, the values attributed to the strength and toughness parameters of the two interfaces under study were obtained from the data presented in [48] and in [50] for the AS4/8552 prepreg and the AFK-163 adhesive layers, respectively, with the exception of the SERR's in Mode I, G_{IC}, which were set to the values obtained by averaging the data reported in Fig. 7. The properties introduced in the CZM's are summarized in Table 3. The properties of the materials are set as reported in Table 1. The adhesive and titanium are considered isotropic, while composite material is defined by engineering constant features in ABAQUS [63]. As an initial option, the B-K criterion with $\eta = 1.45$ was selected to determine the toughness in mixed mode openings.

The resulting models of the specimens are exemplified in the mesh presented in Fig. 9-A. The cooling phase of the manufacturing process and the complete DCB tests, including unloading, were analyzed using the same model in single-step (cooling phase or DCB loading and unloading) and two-step analyses (cooling phase followed by DCB loading and unloading). All analyses were performed with an explicit time integration scheme with Simulia/Abaqus Explicit.

Boundary conditions include two rigid surfaces on the arms at the pre-cracked end of the specimens to apply the velocity boundary conditions in order to simulate the loading and unloading phases in the DCB tests; such surfaces represented the hinge tabs bonded to the arms of the DCB specimens, which are visible in Fig. 5; they were also included in the cooling phase of the two-step analyses; however, it was verified that they influenced the solutions only at the end of the arms and not at the crack tips; moreover, they were left free to move in the cooling phase, so to avoid any interference with the contraction of the whole specimen in the thickness direction.

The cooling analysis started from an initial stress-free temperature identified by means of numerical-experimental correlation with the data acquired by FBG's during the manufacturing cycle, as shown in section 5. In this phase, the temperature decreased to the final temperature of 20 °C during the explicit analyses. DCB opening and unloading were obtained by applying proper velocity boundary conditions to the rigid body reference nodes. Velocity was imposed in the *z*-direction shown in Fig. 9. Rotations about the *y* axis were kept free to represent the hinge. Smooth variations characterized both the imposed temperature and velocity time histories to avoid the excitation of vibrations and perform a quasi-static explicit analysis.

4. Calibration of the numerical model and numerical-experimental correlation

4.1. Analyses of cooling phase in the manufacturing process

In the first phase of the numerical activity, single-step cooling simulations of specimens SC and AC#1 were performed to calibrate and assess the set of CTE's adopted in the models and set a reasonable value for the free-stress temperature used as the initial condition. The identification of such parameters was accomplished by comparing the experimental strain measured by the FBG sensors with the numerical strains evaluated at the same locations.

In the analyses, the CTE of Titanium alloy was kept fixed at $9.0 \cdot 10^{-6}\,°C^{-1}$, while the CTE of the adhesive material was set to $90 \cdot 10^{-6}\,°C^{-1}$, as provided by the material datasheet [50].

Strain vs. temperature curves in the cooling phase were obtained from the experimental data presented in Fig. 10-A. A slope change is apparent between 120 °C and 100 °C, likely to be originated by the different glass transition temperatures the resin in the composite sub-laminates and of the adhesive. According to such interpretation, the slope change indicates the transition of the adhesive material to a more rigid state. Indeed, the glass transition temperature of the adhesive is 108 °C [50].

In the numerical analyses, the absence of viscous behavior, the adoption of constant elastic stiffness, and constant CTE led to obtaining temperature vs. strain curves with a substantially constant slope. Considering the CTE's value adopted in the CLT model presented in section 3.1, the slope was found to be reasonably close to the experimental one in the final phase of the cooling, and the numerical slope was found practically identical for all the FBG locations. However, a sensitivity to the CTE of composite plies in material axes was detected, as exemplified in Fig. 10. Eventually, the values $\alpha_1 = -1.8 \cdot 10^{-6}\,°C^{-1}$ and $\alpha_2 = \alpha_3 = 24 \cdot 10^{-6}\,°C^{-1}$ were selected for the composite material, to approximate more accurately the experimental data.

If 110 °C was chosen as the initial condition in the thermal analyses, the numerical strain levels obtained in the final regime

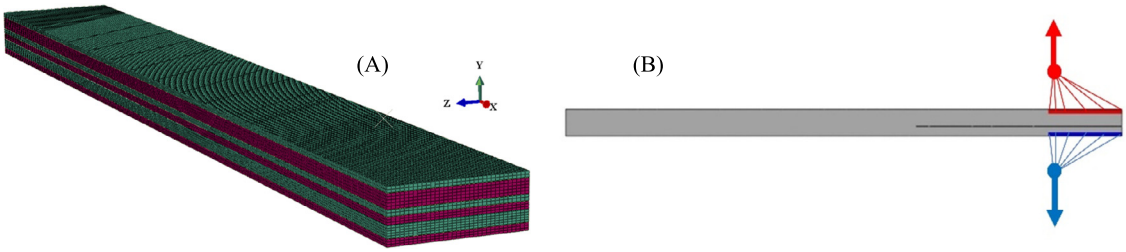

Fig. 9. A) Numerical model of a DCB specimen, and B) scheme for the application of the boundary conditions for DCB opening.

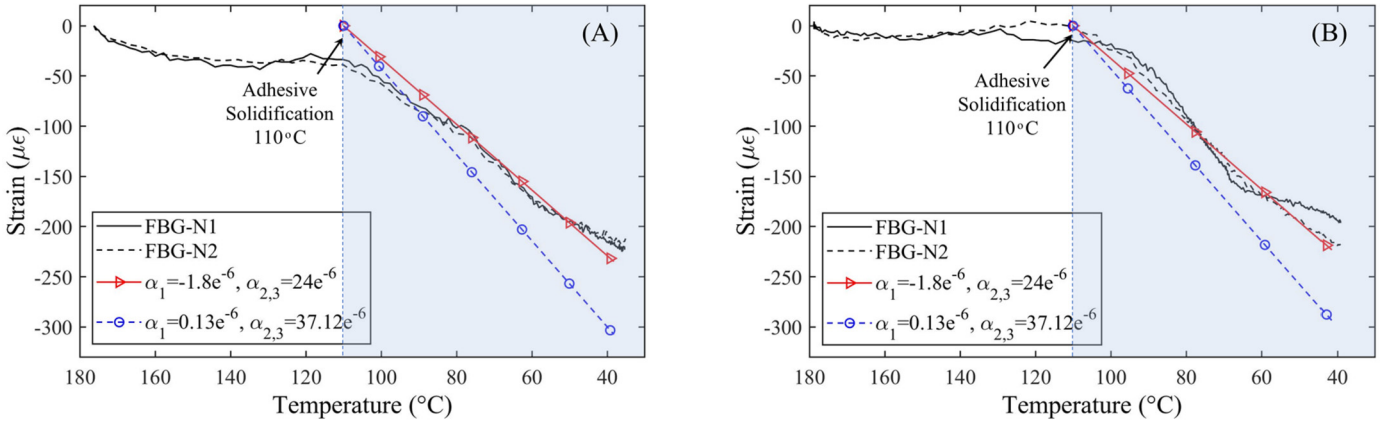

Fig. 10. Numerical-experimental correlation of strain evolution in the cooling phase of A) SC, and B) AC#1 specimens.

of the cooling phase resulted in acceptable agreement with the experimental results both in SC and AC#1 specimens, as shown in Fig. 10. Accordingly, such temperature was selected as the stress-free temperature in the cooling step of the analysis. Both laminations with embedded sensors are equipped with a temperature sensor isolated in a capillary tube adjacent to other FBG sensors in the same layer. Based on the results obtained by this sensor, the temperature inside the laminate is equal to the curing temperature applied by the hot press plate according to MRCC [48], Fig. 3. Such temperature is controlled during the cycle through a thermocouple set on the heated plates. The equivalence between the internal measure acquired by the FBG and the imposed temperature indicates that the temperature gradient is practically null inside the laminate. Therefore, In the numerical simulation, the temperature is set to be uniform in all the elements.

The analyses of the cooling phase performed with the identified CTE's and stress-free temperature made possible an evaluation of the residual stress state in the layered specimens, considering the SC, AC#1, and AC#2 configurations.

Fig. 11 presents the contour of displacement and the final shape of specimens after the cooling phase. In the SC specimen, compressive stress between 70 MPa and 90 MPa was obtained in the composite layers, whereas the tensile stress in titanium alloy was about 70 MPa. Distortions in the zone of the pre-crack were obtained, with gaps of 1.04 mm for AC#1 and 2.06 mm for AC#2 between the two arms at the pre-cracked end of the specimens. The numerical analysis resulted in good qualitative and quantitative agreement with the distortion of physical specimens extracted from the mold and cut (see Fig. 4-B,C). The comparison between the distortion calculated by CLT (Eq. (2)) (with calibrated CTE and from stress-free temperature) and FEM through the length of pre-crack is shown in Fig. 11. The total distortion in this plot means the distance between two arms after cooling. The trend of curvature is similar in both assessment methods. The total distortion obtained by FEM has less than a 5 percent difference with experimental results. The CLT results show an acceptable approximation for predicting the distortion. However, the boundary condition of the two arms and the 3D stress state at the crack tip can not be reproduced with the same accuracy of FEM.

Additional results of the thermal analyses are reported in Fig. 12, where the plots of interlaminar stresses in the vicinity of the crack tip, at the edges, and in the middle of the specimens are shown. These curves are related to the stress at 20 °C, at the end of the cooling phase. As shown in Fig. 12-D, two through-the-thickness paths are defined: path.1, located at the edge of the specimen, and path.2 in the middle.

The values reported in Fig. 12-A are referred to the SC specimen. As expected, the stress value in the middle of the specimen and exactly at the pre-crack tip was negligible; however, edge effects included a normal stress component σ_{33} with a maximum absolute value of about 8 MPa as well as τ_{23} components. In the numerical simulation, the stress at the edges was below the damage initiation threshold in adhesive layers according to the data reported in Fig. 12 and to the strength criterion expressed in Eq. (10).

The results of the numerical analysis on the AC#1 and AC#2 specimens are reported in Fig. 12-B and Fig. 12-C, respectively. The stress originating from the edge effects along the border of the specimens acting in the adhesive layers was very similar to those obtained in the SC specimen. However, the stress obtained in the numerical solution at the crack tip was not negligible for both asymmetrically cracked specimens. In the AC#1 specimen, stress σ_{33} of about 10 MPa, shear stress τ_{13} of 15 MPa were obtained along the crack front, with an additional component τ_{23} of 15 MPa at the intersection between the crack front and the lateral edge of the specimens (see Fig. 12-C). Such stress values were transmitted through the layer of solid elements representing the adhesive. Similar values were also obtained in AC#2, where stress was transmitted through an internal interlaminar layer of the composite sub-laminate, modeled by using conventional cohesive elements (see Fig. 12-B). However, in the numerical simulation, these values did not exceed the threshold for damage initiation defined by the strength criterion; it should be observed that the numerical stress state at the discontinuity represented by the crack tip is expected to be highly mesh-dependent. In addition, the strength properties

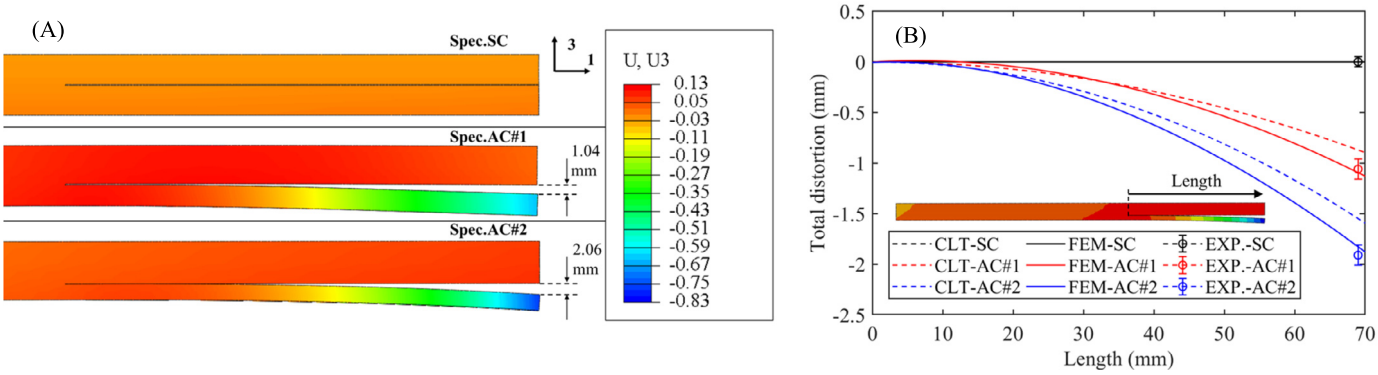

Fig. 11. A) Contour of distortion and B) comparison of distortion obtained from CLT, FEM, and experimental results in SC, AC#1, and AC#2.

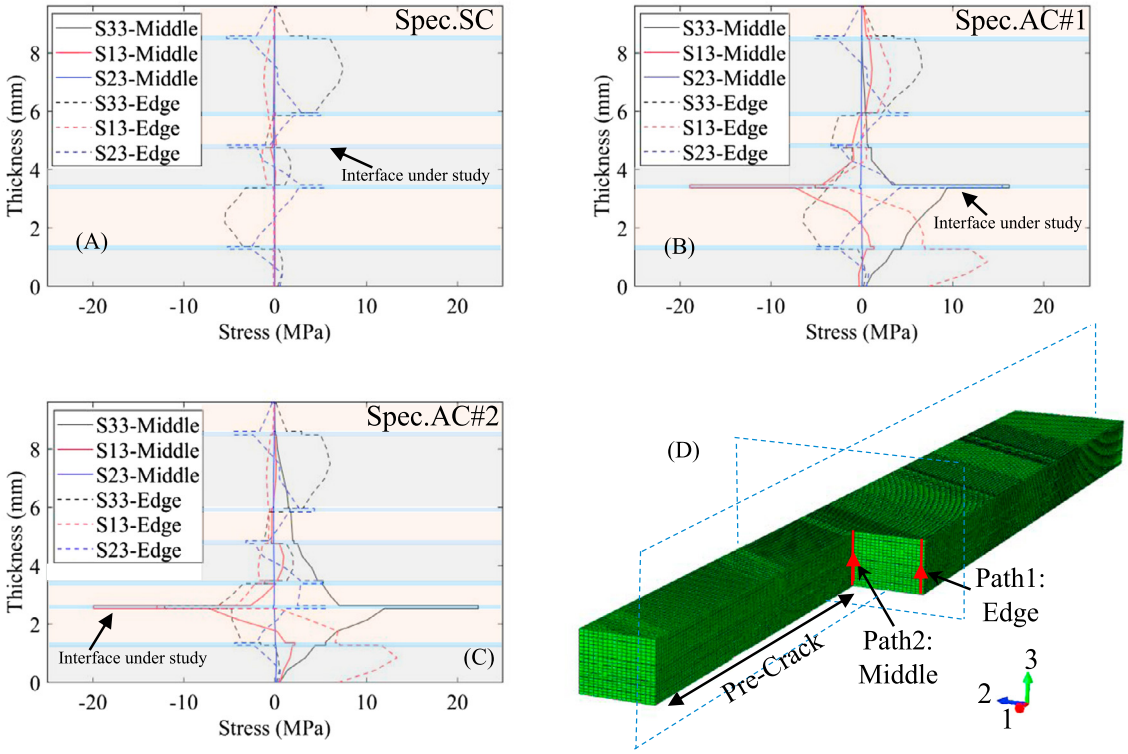

Fig. 12. Numerical stress contours of A) SC, B) AC#1, and C) AC#2 specimens after Cooling simulation.

of the interface layer could vary significantly with the temperature. Therefore, the values reported indicating the development of a significant stress state at the pre-crack tip during the manufacturing cycle, with possible effects on the mechanical properties.

4.2. Analyses of DCB tests and effects of residual stress on the response

The numerical simulations of DCB loading and unloading cycles were performed by adopting the same finite element models of thermal analyses. Two types of analysis were conducted. In the first type of procedure, a single-step analysis was performed by applying the velocity boundary conditions to the reference nodes representing the hinges to model the DCB opening without performing a preliminary thermal analysis. In the second procedure, a complete two-step analysis scheme was applied, with an initial cooling step followed by the application of velocity boundary conditions in order to simulate DCB loading and unloading phases. The initial thermal analysis was conducted with the same parameters and initial conditions identified in the previous section.

In both the single-step and two-step procedures, the vertical velocity applied to the reference nodes of the hinges was reverted after the opening of the specimen until a desired amount of displacement to simulate the unloading response of the specimen and evaluate the residual displacements. Moreover, numerical strains were compared with the data acquired by the embedded FBG sensors in SC and AC#1 specimens.

The comparison of numerical and experimental results of load versus displacement in the SC specimen is presented in Fig. 13-A. It can be observed the results obtained with and without the preliminary cooling analysis are superimposed and are in good agreement with the experimental results both in the opening and in the unloading phase. The strains measured by the FBG's embedded in the specimen are plotted in Fig. 13-B against the opening of the DCB arms and are compared with the numerical results. The closest sensor to the pre-crack tip was in identical positions in the specimen (at 16 mm from the crack tip before pre-opening). It provided a very similar experimental curve, characterized by a change of slope at the onset of crack propagation. Numerical results are identical for both single-step and two-step procedures and capture

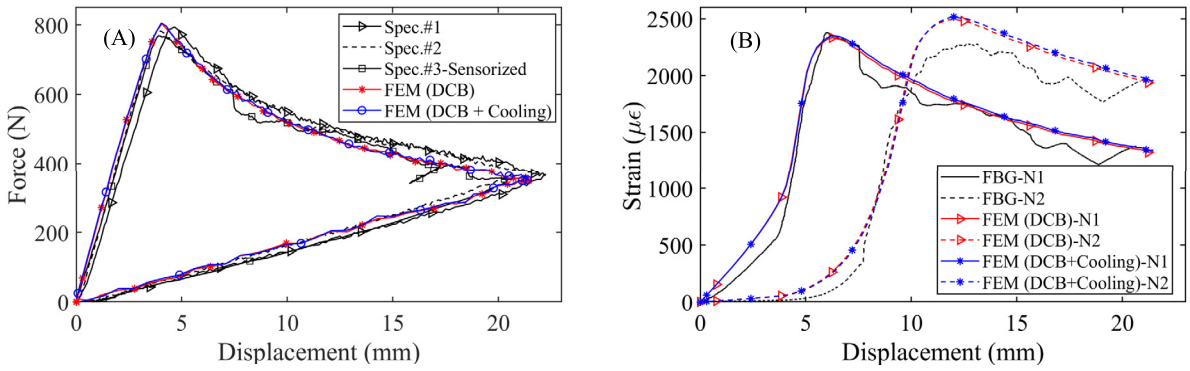

Fig. 13. Numerical-experimental correlation of A) overall force vs. displacement response and B) internal strain evaluation in SC specimen.

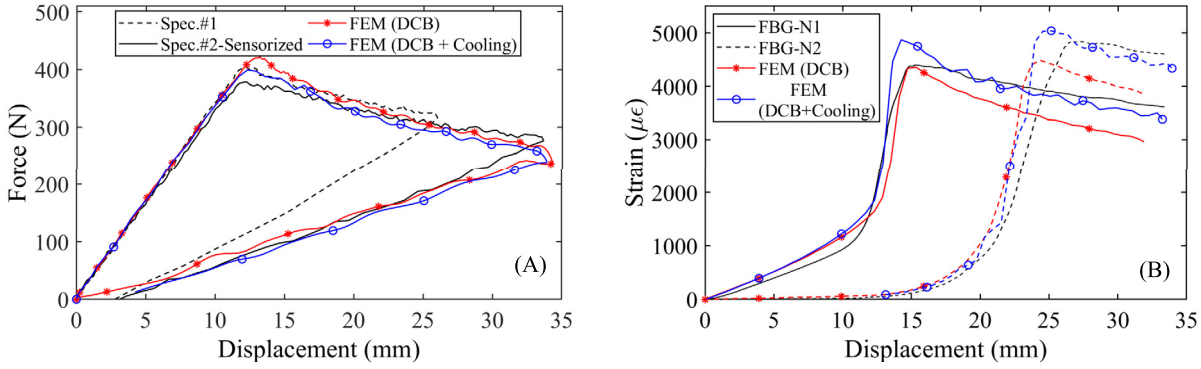

Fig. 14. A) Numerical–experimental correlation of force vs. displacement response in AC#1 specimen and B) distribution of toughness in the modified model of AC#1 specimen.

the experimental trend with a discrepancy of less than 3 percent after the onset of crack. In the second sensor, the numerical strain signal is in agreement with the experimental one in the raising phase though the maximum level is not well captured. The numerical approach overestimated the strain by about 10 percent. However, a generally acceptable correlation was obtained at the level of local strain during crack propagation, and the equivalence between the numerical responses obtained with and without the thermal analyses confirm that the residual stress did not influence the DCB tests evaluated SERR.

In the numerical analyses performed on the AC#1 configuration, the response of the first opening overestimated the experimental data both in the single-step and two-steps analyses. Such overestimation can be attributed to the possible effects of the stress states, and the distortions developed at the crack tip during manufacturing. However, since the investigation of these phenomena is beyond the scope of the paper, the numerical activity focused on the second opening phase.

The opening of Spec#1 is stopped when the displacement is reached 25 mm. Since the FBG#2 in Spec#2 was located far from the pre-crack, the opening continued until the sensor collected the strain evolution during the crack propagation. The small discrepancies between the experimental results of the two specimens could be attributed to the statistical variation of material properties since they follow the identical trend in force-displacement.

The numerical-experimental correlation of the force vs. displacement response obtained considering the AC#1 response in the second opening phase is presented in Fig. 14. Despite the development of additional permanent displacement in this phase, as indicated by the experimental evidence, it can be observed that slight differences of 20 N were captured in the numerical responses obtained with the two different procedures, which is reduced to 5 N as crack growth. However, the permanent deflection developed at

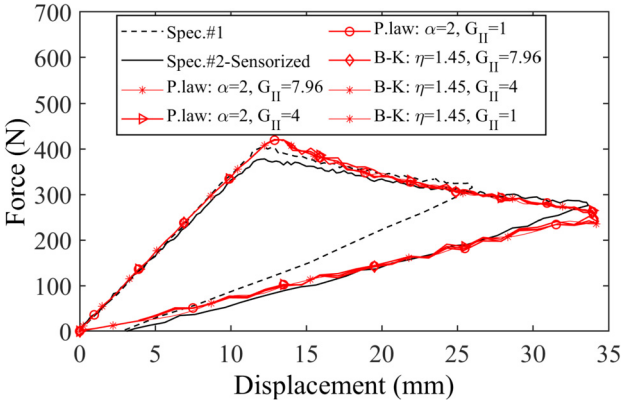

Fig. 15. Comparison between power-law and B-K criterion in respect with different Mode II toughness values and different toughness criteria.

the end of unloading is captured only in the procedure, including the cooling step and the residual thermal stress. Indeed, the DCB analysis performed after the thermal analysis correctly predicted the occurrence of a residual displacement of 3.5 mm at the complete unloading, which was in good agreement with the experimental results.

Moreover, the presence of residual stress significantly influenced the numerical strain at the local level, as shown in Fig. 14-B, referred to the numerical-experimental correlation of the internal strain evolution along with the sensors. Indeed, the numerical analysis performed with the preliminary cooling step increased the maximum strains at the FBG location during the opening phase by about 20%, thus leading to an appreciable agreement with the experimental data. However, it can be observed that, for the second sensor, FBG-N2, the correspondence between the raising phase of the strain and the DCB opening is not in perfect agreement with

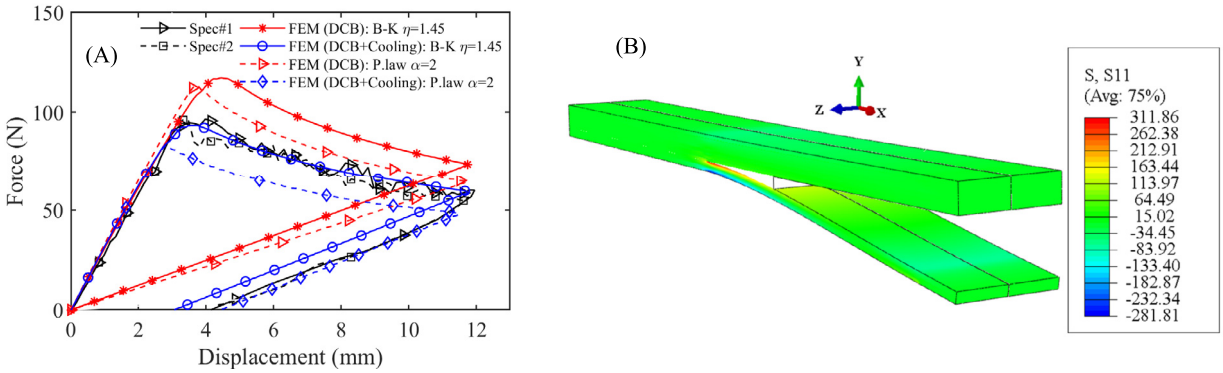

Fig. 16. A) Numerical-experimental correlation of the force vs. displacement curves in AC#2 configuration and B) contour of σ_{11} in the numerical analysis during the opening phase.

the experimental data. The experimental scattering between the responses, which is higher than for the SC specimens, could be considered responsible for such discrepancy.

However, the shape and the maximum strain levels of the strain vs. displacement curves obtained in the two-step analysis are in good agreement with the experimental results, whereas the strains evaluated without preliminary thermal analysis underestimate the maximum experimental strains systematically. It is also worth noting that the two-step analysis, including residual thermal stress, correctly captured the permanent deflection at the end of the unloading phase.

Since the AC#1 test could not be considered in pure Mode I, a sensitivity study was performed to investigate the role of Mode II characterization on the propagation due to the asymmetry between the arms. Fig. 15 presents the comparison between the analyses performed B-K ($\eta = 1.45$) and power-law toughness criterion ($\beta = 2$), with different values of G_{IIc} (1 kJ/m^2, 4 kJ/m^2, and 7.96 kJ/m^2). Results show negligible differences, thus indicating that the effect of Mode II propagation is insignificant. Similar results were also obtained for the strain data, which are omitted for the sake of brevity.

Overall, the numerical investigation indicates that, for the AC#1 specimens, the presence of residual thermal stress did not significantly affect the forces required for crack propagation, although it led to significant permanent displacements and modified the evolution of strain fields during the test.

The analyses of specimen AC#2 were conducted considering initial crack lengths and maximum openings corresponding to those of the two tests reported in Fig. 6-C, which were characterized by a significant final permanent displacement at the unloading of almost 4 mm. Such analyses provided the most interesting results regarding the influence of the residual stress on the force required to propagate an interface fracture and the influence of mixed-mode propagation. Indeed, the force versus displacement response obtained without considering the thermal stress overestimates the experimental force, particularly if the B-K law is adopted, as shown in Fig. 16-A. Moreover, the development of residual permanent opening at unloading is not represented. The introduction of the thermal analysis step calibrated thanks to the monitoring of the cycle provided by the optical fibers, obtained an appreciable numerical-experimental correlation for the analysis with B-K toughness criterion, regarding the opening phase, and a good estimation of residual displacement at unloading for both B-K and power-law criterion, as shown in Fig. 16-A. The difference between the numerical approach of with and without the thermal analyses captured the residual thermal stress of about 50 N, approximately 30 percent of maximum fracture force. The picture in Fig. 16-B is referred to as the contour of σ_{11} in the analysis and can be compared with Fig. 5-C to confirm the correlation with the deformed shape. Hence, the analysis adopting the B-K criterion and including a preliminary cooling step could capture both loading and unloading phases of the experimental tests. The remarkable effect of the residual stress on the force required for damage propagation at interfaces within the composite sub-laminates rather than in the adhesive interface between the different materials can also be underlined.

Overall, the numerical-experimental correlations presented in this section confirmed the validity of the thermal model calibration achieved by using the data acquired by the FBG sensors. Results also validate the embedment of CZM into finite thickness elements and highlight the potential of optical fiber based strain monitoring for an accurate assessment of CZM. It can also be observed that the approach proposed led to developing reliable models to study at the global and local levels cases with significantly different and increasing influence of the residual stress state on the damage propagation at all the interfaces of hybrid specimens.

5. Conclusions

In this paper, the build-up of residual stress in hybrid specimens and the consequence on the propagation of damage at interfaces were investigated using specifically designed specimens, equipped with a strain monitoring system, and developing numerical models validated both at the local and the global levels.

The results obtained from all three specimens validated the proposed technique for controlling residual thermal stress on the hybrid specimen. Thanks to this technique, the SC specimen is designed residual stress-free to calibrate the numerical tool and assess Mode I toughness of adhesive interface between dissimilar materials.

The introduction of the monitoring system based on FBG sensors carried by optical fibers proved to be a valuable tool for investigating manufacturing cycles and identifying parameters such as material CTE and stress-free temperature. Moreover, FBG's provided a measure of the strain evolution during crack propagation, providing essential data to validate the numerical analyses. The integration between the optical fiber-based monitoring systems and the numerical procedures made possible the development of models able to capture the residual stress state reliably in the hybrid structural elements and model their effects on the crack propagation. The numerical investigations point out that the most significant effects of residual stress build-up in hybrid composite/metallic specimens have affected delaminations that occurred inside composite sub-laminates, which have relatively low toughness levels.

The experimental-numerical procedures applied in this work can be considered an efficient protocol to develop, calibrate, and validate reliable numerical models to analyze and predict struc-

tural integrity and damage tolerance in real-world hybrid composite/metallic structures

Declaration of competing interest

The authors declare that they have no known competing financial interests or personal relationships that could have appeared to influence the work reported in this paper.

Acknowledgement

The authors thank Plyform Composites s.r.l. and Aerea S.p.A for the material provided, Ing. Lorenzo Cartabia of Plyform Composite s.r.l. and Ing. Matteo Stella for the contribution in this work. This project has received funding from the European Union's H2020 research and innovation program under the Marie Skłodowska-Curie grant agreement No. 721920.

References

[1] A. Vlot, J.W. Gunnink, Fibre Metal Laminates: An Introduction, Springer Science & Business Media, 2011.
[2] J. Ludick, T. Raman, Industrialization of a carbon composite control rod, in: Proceedings of International Conference on Composite Materials, ICCM-12, Paris, 1999.
[3] V. Mara, R. Haghani, M. Al-Emrani, Improving the performance of bolted joints in composite structures using metal inserts, J. Compos. Mater. 50 (21) (2016) 3001–3018, https://doi.org/10.1177/0021998315615204.
[4] P.P. Camanho, A. Fink, A. Obst, S. Pimenta, Hybrid titanium–CFRP laminates for high-performance bolted joints, Composites, Part A, Appl. Sci. Manuf. 40 (12) (2009) 1826–1837, https://doi.org/10.1016/j.compositesa.2009.02.010.
[5] D.H. Cho, D.G. Lee, Manufacturing of co-cured composite aluminum shafts with compression during co-curing operation to reduce residual thermal stresses, J. Compos. Mater. 32 (12) (1998) 1221–1241, https://doi.org/10.1177/002199839803201205.
[6] H.S. Kim, J.W. Kim, J.K. Kim, Design and manufacture of an automotive hybrid aluminum/composite drive shaft, Compos. Struct. 63 (1) (2004) 87–99, https://doi.org/10.1016/S0263-8223(03)00136-3.
[7] P. Tsokanas, T. Loutas, P. Nijhuis, Interfacial fracture toughness assessment of a new titanium–CFRP adhesive joint: an experimental comparative study, Metals 10 (5) (2020) 699, https://doi.org/10.3390/met10050699.
[8] H.S. Kim, Reduction of fabricational thermal residual stress of the hybrid co-cured structure using a dielectrometry, Compos. Sci. Technol. 67 (1) (2007) 29–44, https://doi.org/10.1016/j.compscitech.2006.05.002.
[9] H.S. Kim, S.W. Park, Smart cure cycle with cooling and reheating for co-cure bonded steel/carbon epoxy composite hybrid structures for reducing thermal residual stress, Composites, Part A, Appl. Sci. Manuf. 37 (10) (2006) 1708–1721, https://doi.org/10.1016/j.compositesa.2005.09.015.
[10] ASTM International D5528-13, Standard Test Method for Mode I Interlaminar Fracture Toughness of Unidirectional Fiber-Reinforced Polymer Matrix Composites, ASTM International, West Conshohocken, 2013.
[11] W. Wang, R.L. Fernandes, S.T. De Freitas, D. Zarouchas, R. Benedictus, How pure mode I can be obtained in bi-material bonded DCB joints: a longitudinal strain-based criterion, Composites, Part B, Eng. 153 (2018) 137–148, https://doi.org/10.1016/j.compositesb.2018.07.033.
[12] H. Orsini, F. Schmit, Influence of residual thermal stresses on the fracture behavior of hybrid bonded joints, J. Adhes. 43 (1–2) (1993) 55–68, https://doi.org/10.1080/00218469308026587.
[13] J. Jiao, C. Gurumurthy, E. Kramer, Y. Sha, C. Hui, P. Borgesen, Measurement of interfacial fracture toughness under combined mechanical and thermal stresses, J. Electron. Packag. 120 (4) (1998) 349–353, https://doi.org/10.1115/1.2792645.
[14] T. Yokozeki, Energy release rates of bi-material interface crack including residual thermal stresses: application of crack tip element method, Eng. Fract. Mech. 77 (1) (2010) 84–93, https://doi.org/10.1016/j.engfracmech.2009.09.018.
[15] P. Tsokanas, T. Loutas, G. Kotsinis, V. Kostopoulos, W.M. van den Brink, F.M. de la Escalera, On the fracture toughness of metal-composite adhesive joints with bending-extension coupling and residual thermal stresses effect, Composites, Part B, Eng. 185 (2020) 1076–1094, https://doi.org/10.1016/j.compositesb.2019.107694.
[16] Z. Ouyang, G. Ji, G. Li, On approximately realizing and characterizing pure mode-I interface fracture between bonded dissimilar materials, J. Appl. Mech. 78 (3) (2011) 310–320, https://doi.org/10.1115/1.4003366.
[17] S.A. Faghidian, Inverse determination of the regularized residual stress and eigenstrain fields due to surface peening, J. Strain Anal. Eng. Des. 50 (2) (2015) 84–91, https://doi.org/10.1177/0309324714558326.
[18] G. Farrahi, S. Faghidian, D. Smith, An inverse method for reconstruction of the residual stress field in welded plates, J. Press. Vessel Technol. 132 (6) (2010) 061205, https://doi.org/10.1115/1.4001268.
[19] G. Farrahi, S. Faghidian, D. Smith, An inverse approach to determination of residual stresses induced by shot peening in round bars, Int. J. Mech. Sci. 51 (9–10) (2009) 726–731, https://doi.org/10.1016/j.ijmecsci.2009.08.004.
[20] S. Ali Faghidian, Analytical inverse solution of eigenstrains and residual fields in autofrettaged thick-walled tubes, J. Press. Vessel Technol. 139 (3) (2017) 031205, https://doi.org/10.1115/1.4034675.
[21] S. Ali Faghidian, Analytical approach for inverse reconstruction of eigenstrains and residual stresses in autofrettaged spherical pressure vessels, J. Press. Vessel Technol. 139 (4) (2017) 041202, https://doi.org/10.1115/1.4035980.
[22] J.A. Nairn, Fracture mechanics of composites with residual thermal stresses, J. Appl. Mech. 64 (4) (1997) 804–810, https://doi.org/10.1115/1.2788985.
[23] J.A. Nairn, Energy release rate analysis for adhesive and laminate double cantilever beam specimens emphasizing the effect of residual stresses, Int. J. Adhes. Adhes. 20 (1) (2000) 59–70, https://doi.org/10.1016/S0143-7496(99)00016-0.
[24] T. Yokozeki, T. Ogasawara, T. Aoki, Correction method for evaluation of interfacial fracture toughness of DCB, ENF and MMB specimens with residual thermal stresses, Compos. Sci. Technol. 68 (3–4) (2008) 760–767, https://doi.org/10.1016/j.compscitech.2007.08.025.
[25] P. Tsokanas, T. Loutas, Hygrothermal effect on the strain energy release rates and mode mixity of asymmetric delaminations in generally layered beams, Eng. Fract. Mech. 214 (2019) 390–409, https://doi.org/10.1016/j.engfracmech.2019.03.006.
[26] S.B. Cox, L.C. Tate, S.E. Danley, J.W. Sampson, B.J. Taylor, J.K. Sutter, S.G. Miller, Stress free temperature testing and calculations on out-of-autoclave composites, in: SAMPE Conference, Long Beach, CA, 2013.
[27] P. Prasatya, G.B. McKenna, S.L. Simon, A viscoelastic model for predicting isotropic residual stresses in thermosetting materials: effects of processing parameters, J. Compos. Mater. 35 (10) (2001) 826–848, https://doi.org/10.1177/a037322.
[28] A. Johnston, R. Vaziri, A. Poursartip, A plane strain model for process-induced deformation of laminated composite structures, J. Compos. Mater. 35 (16) (2001) 1435–1469, https://doi.org/10.1106/YXEA-5MH9-76J5-BACK.
[29] N. Zobeiry, R. Vaziri, A. Poursartip, Computationally efficient pseudo-viscoelastic models for evaluation of residual stresses in thermoset polymer composites during cure, Composites, Part A, Appl. Sci. Manuf. 41 (2) (2010) 247–256, https://doi.org/10.1016/j.compositesa.2009.10.009.
[30] H. Darvishgohari, M. Zarastvand, R. Talebitooti, R. Shahbazi, Hybrid control technique for vibroacoustic performance analysis of a smart doubly curved sandwich structure considering sensor and actuator layers, J. Sandw. Struct. Mater. 23 (5) (2019), https://doi.org/10.1177/1099636219896251.
[31] R. Talebitooti, H. Darvish Gohari, M. Zarastvand, A. Loghmani, A robust optimum controller for suppressing radiated sound from an intelligent cylinder based on sliding mode method considering piezoelectric uncertainties, J. Intell. Mater. Syst. Struct. 30 (20) (2019) 3066–3079, https://doi.org/10.1177/1045389X19873412.
[32] H. Gohari, M. Zarastvand, R. Talebitooti, A. Loghmani, M. Omidpanah, Radiated sound control from a smart cylinder subjected to piezoelectric uncertainties based on sliding mode technique using self-adjusting boundary layer, Aerosp. Sci. Technol. 106 (2020) 106141, https://doi.org/10.1016/j.ast.2020.106141.
[33] G. Sala, L. Di Landro, A. Airoldi, P. Bettini, Fibre optics health monitoring for aeronautical applications, Meccanica 50 (10) (2015) 2547–2567, https://doi.org/10.1007/s11012-015-0200-6.
[34] I. García, J. Zubia, G. Durana, G. Aldabaldetreku, M.A. Illarramendi, J. Villatoro, Optical fiber sensors for aircraft structural health monitoring, Sensors 15 (7) (2015) 15494–15519, https://doi.org/10.3390/s150715494.
[35] J.R. Dunphy, G. Meltz, F. Lamm, W.W. Morey, Multifunction, distributed optical fiber sensor for composite cure and response monitoring, in: Fiber Optic Smart Structures and Skins III, 1990.
[36] M. Giordano, A. Laudati, J. Nasser, L. Nicolais, A. Cusano, A. Cutolo, Monitoring by a single fiber Bragg grating of the process induced chemo-physical transformations of a model thermoset, Sens. Actuators A, Phys. 113 (2) (2004) 166–173, https://doi.org/10.1016/j.sna.2004.02.033.
[37] Y. Wang, B. Han, A. Bar-Cohen, S. Cho, Fiber Bragg grating sensor to characterize curing process-dependent mechanical properties of polymeric materials, in: 2007 Proceedings 57th Electronic Components and Technology Conference, IEEE, 2007, pp. 1045–1050.
[38] L. Sorensen, T. Gmür, J. Botsis, Residual strain development in an AS4/PPS thermoplastic composite measured using fibre Bragg grating sensors, Composites, Part A, Appl. Sci. Manuf. 37 (2) (2006) 270–281, https://doi.org/10.1016/j.compositesa.2005.02.016.
[39] C.-C. Chiang, P. Tesinova, Curing monitoring of composite material using embedded fiber Bragg grating sensors, in: Advances in Composite Materials-Analysis of Natural and Man-Made Materials, 2011, pp. 345–360.
[40] M. Mulle, F. Collombet, P. Olivier, Y.-H. Grunevald, Assessment of cure residual strains through the thickness of carbon–epoxy laminates using FBGs, part I: elementary specimen, Composites, Part A, Appl. Sci. Manuf. 40 (10) (2009) 94–104, https://doi.org/10.1016/j.compositesa.2009.06.013.

[41] S.S. Kim, H. Murayama, K. Kageyama, K. Uzawa, M. Kanai, Study on the curing process for carbon/epoxy composites to reduce thermal residual stress, Composites, Part A, Appl. Sci. Manuf. 43 (8) (2012) 1197–1202, https://doi.org/10.1016/j.compositesa.2012.02.023.
[42] H.-K. Kang, D.-H. Kang, H.-J. Bang, C.-S. Hong, C.-G. Kim, Cure monitoring of composite laminates using fiber optic sensors, Smart Mater. Struct. 11 (2) (2002) 279–287, https://doi.org/10.1088/0964-1726/11/2/311.
[43] R. Prussak, D. Stefaniak, C. Hühne, M. Sinapius, Evaluation of residual stress development in FRP-metal hybrids using fiber Bragg grating sensors, Prod. Eng. 12 (2018) 259–267, https://doi.org/10.1007/s11740-018-0793-4.
[44] A. Airoldi, C. Mirani, L. Principito, A bi-phasic modelling approach for interlaminar and intralaminar damage in the matrix of composite laminates, Compos. Struct. 234 (2020) 111747, https://doi.org/10.1016/j.compstruct.2019.111747.
[45] A. Airoldi, G. Sala, P. Bettini, A. Baldi, An efficient approach for modeling interlaminar damage in composite laminates with explicit finite element codes, J. Reinf. Plast. Compos. 32 (15) (2013) 1075–1091, https://doi.org/10.1177/0731684412473004.
[46] A. Airoldi, A. Baldi, P. Bettini, G. Sala, Efficient modelling of forces and local strain evolution during delamination of composite laminates, Composites, Part B, Eng. 72 (2015) 137–149, https://doi.org/10.1016/j.compositesb.2014.12.002.
[47] (Accessed 14 December 2021), https://www.wichita.edu/industry_and_defense/NIAR/Research/ncamp.php.
[48] K. Marlett, Y. Ng, J. Tomblin, Hexcel 8552 IM7 unidirectional prepreg 190 gsm & 35% RC qualification material property data report, Test Report CAM-RP-2009-015, Rev. A, National Center for Advanced Materials Performance, Wichita, Kansas, 2011, pp. 1–238.
[49] Titanium Ti-6Al-4V (Grade 5), Annealed, http://asm.matweb.com/search/SpecificMaterial.asp?bassnum=mtp641. (Accessed 17 November 2021).
[50] 3M™ Scotch-Weld, Structural Adhesive Film AF 163-2, November 2009.
[51] R.M. Jones, Mechanics of Composite Materials, CRC Press, 1998.
[52] I.M. Daniel, O. Ishai, I.M. Daniel, I. Daniel, Engineering Mechanics of Composite Materials, Oxford University Press, New York, 2006.
[53] H.-S. Kim, S.-H. Yoo, S.-H. Chang, In situ monitoring of the strain evolution and curing reaction of composite laminates to reduce the thermal residual stress using FBG sensor and dielectrometry, Composites, Part B, Eng. 44 (1) (2013) 446–452, https://doi.org/10.1016/j.compositesb.2012.04.021.
[54] S. Minakuchi, In situ characterization of direction-dependent cure-induced shrinkage in thermoset composite laminates with fiber-optic sensors embedded in through-thickness and in-plane directions, J. Compos. Mater. 49 (9) (2015) 1021–1034, https://doi.org/10.1177/0021998314528735.
[55] S. Minakuchi, S. Niwa, K. Takagaki, N. Takeda, Composite cure simulation scheme fully integrating internal strain measurement, Composites, Part A, Appl. Sci. Manuf. 84 (2016) 53–63, https://doi.org/10.1016/j.compositesa.2016.01.001.
[56] K. Takagaki, S. Minakuchi, N. Takeda, Process-induced strain and distortion in curved composites. Part I: development of fiber-optic strain monitoring technique and analytical methods, Composites, Part A, Appl. Sci. Manuf. 103 (2017) 219–229, https://doi.org/10.1016/j.compositesa.2017.09.019.
[57] P. Hubert, G. Fernlund, A. Poursartip, Autoclave processing for composites, in: Manufacturing Techniques for Polymer Matrix Composites (PMCs), Elsevier, 2012, pp. 414–434.
[58] C. Sarrado, F.A. Leone, A. Turon, Finite-thickness cohesive elements for modeling thick adhesives, Eng. Fract. Mech. 168 (2016) 105–113, https://doi.org/10.1016/j.engfracmech.2016.03.020.
[59] A. Baldi, A. Airoldi, M. Crespi, P. Iavarone, P. Bettini, Modelling competitive delamination and debonding phenomena in composite T-joints, Proc. Eng. 10 (2011) 3483–3489, https://doi.org/10.1016/j.proeng.2011.04.574.
[60] M.L. Benzeggagh, M. Kenane, Measurement of mixed-mode delamination fracture toughness of unidirectional glass/epoxy composites with mixed-mode bending apparatus, Compos. Sci. Technol. 56 (4) (1996) 439–449, https://doi.org/10.1016/0266-3538(96)00005-X.
[61] S. Cardamone, A. Bernasconi, M. Giglio, Characterization of the 3M Scotch-Weld™ 7260 B/A epoxy adhesive by cohesive damage models and application to a full-scale bonded sub-structure, J. Adhes. 96 (14) (2020) 1270–1301, https://doi.org/10.1080/00218464.2019.1591278.
[62] P.P. Camanho, C.G. Davila, M. De Moura, Numerical simulation of mixed-mode progressive delamination in composite materials, J. Compos. Mater. 37 (16) (2003) 1415–1438, https://doi.org/10.1177/0021998303034505.
[63] Abaqus® 6.11 Documentation, Analysis User's Guide, Volume IV: Elements, Dassault Systemes Simulia Corp., Providence (RI, USA), 2011.